Contact mechanics and friction of soft materials: an instrument combining multi-axes dynamical actuation/measurement and in situ visualisation

A. Aymard,[1, a)] C. Oliver,[1, a)] M. Guibert,[1, a)] T. Durand,[1] M. Leochmach,[2] L. Vanel,[2] D. Dalmas,[1] and J. Scheibert[1, b)]

[1)] *CNRS, Ecole Centrale de Lyon, ENTPE, Laboratoire de Tribologie et Dynamique des Systèmes LTDS, UMR 5513, F-69134, Ecully, France*

[2)] *Université de Lyon, Université Claude Bernard Lyon 1, CNRS, Institut Lumière Matière, F-69622, Villeurbanne, France*

The mechanics and friction of contact interfaces involving soft materials like gel, rubber or human skin, is of both fundamental and applied interest. Recent insights have been made into this field thanks to *in situ* observations of the contact interface. However, current soft-material–oriented tribometers enable only few degrees of freedom for the actuation of the contact, far from covering the richness of the loading conditions applied to real contacts. Here, we introduce an instrument dedicated to the study of the contact mechanics and friction of soft materials which, in addition to *in situ* optical monitoring of the interface, enables simultaneous actuation along five degrees of freedom: three translations and two rotations. All three translations can combine large velocity/large stroke motion and high frequency/small amplitude vibrations. The contact's dynamical response is monitored using both a 6-axes force/torque sensor and a 6-axes displacement/rotation sensor. We successively describe the structure of the instrument, its implementation and alignment, its calibration and resolutions. The capabilities of the instrument are illustrated through two types of experiments on elastomer contacts. Our instrument will be useful to investigate the mechanics of a wide range of interfaces submitted to rich kinematic or dynamic stimuli.

I. INTRODUCTION

Contact interfaces involving soft materials are ubiquitous. For instance, the elastomers of shoe soles[1], tires[2], artificial fingers[3] or robotic grasping tools[4] are used everyday for their high friction-stress against a variety of counter-surfaces. Also, contact with our tongue and skin is central to the tactile perception of food inside the mouth[5] and of surface roughness[6], respectively. Yet, the mechanical and frictional properties of such contacts are complex and remain insufficiently understood (see Ref. 7 and 8 for recent reviews). The scientific challenges stem from an intricate combination of various distinctive behaviours of both the bulk and the interface of soft materials.

First, due to their large compliance and strong adhesion, soft materials usually form relatively large contact areas[9]. Those large areas are not only responsible for the large related friction forces[10], but they are also relatively easy to observe. And indeed, many advances in the field have been made thanks to *in situ* imaging of the contact interface (see e.g. Refs. 10–18).

Second, soft materials are often viscoelastic, which is responsible for, among others, velocity-dependent friction[19,20] and aging[21]. To better understand the role of viscosity on a soft contact, it is thus desirable to vibrate it with controlled frequencies, amplitudes, waveforms and/or directions (compression and/or shear). Experiments where soft contacts are vibrated have investigated either the viscoelastic moduli of the contacting materials[22–24], or the effects of viscoelasticity on the contact properties, e.g. its stiffness[25] or its adhesion energy[26]. In the above mentioned literature works, vibrations were applied along a single direction, normal to the contact, while vibrations along the tangential directions would likely provide important information about the frictional properties of the contact interface[27].

Third, the current state of a soft contact is strongly loading-path–dependent, due to high adhesion[28] and/or friction[29]. To investigate such memory effects, it is thus desirable to be able to apply complex, multi-axes stimuli to the contact. Such capability would for instance enable experimental tests of theoretical predictions[29,30] or reproduction of loading histories relevant to various applications, including tire wear[31] and gecko locomotion[32]. The available loading histories should enable significant negative normal loads, which can occur due to the combination of a large adhesion and a small elastic modulus, and under which friction forces continue to be active[33].

In this context, the scope of this article is to introduce and qualify a new contact-mechanics–oriented instrument capable of addressing a wider range of the above soft-contact–related scientific challenges than any single instrument of the current literature. As we will see, our (remotely operable and programmable) instrument features (i) dynamic actuation of a soft contact along five independent degrees of freedom simultaneously, (ii) monitoring of the six components of the forces/torques applied on the contact, (iii) monitoring of the six displacements/rotations of one of the two solids in contact and (iv) *in situ* imaging of the contact interface.

We will describe the design and technical choices used to build the instrument (section II), its alignment and calibration (section III), before illustrating its capabil-

[a)] These three authors contributed equally to the work

[b)] Correspondance should be addressed to: julien.scheibert@cnrs.fr

ities through a series of experiments involving various elastomer-based contacts (section IV).

II. DESCRIPTION OF THE INSTRUMENT

A. Structure

Figure 1 shows the structure of the instrument. It is built around a couple of sample holders (labels 5 and 6 in Fig. 1) in which the two surfaces of tribological interest can be fixed.

The lower sample holder (label 6) is placed on top of a stack of motorized actuators, so that those massive and opaque parts are as close as possible to the table (1) and do not impede observation of the contact interface from the top. A high precision XY servomotor translation stage (label 9 ; Allio AI-LM-10000-XY) is directly fixed on the table (1), and enables translations in the range ±50 mm with an accuracy ±3 µm and a repetability of ±30 nm, and with speed ranging from 1 µm/s up to 0.8 m/s. On top of this stage is placed a high load capacity XYZ piezoelectric translation stage (8 ; Jena, Tritor 320) enabling high precision motions (repetability better than 1 nm) of amplitude 50, 50 and 400 µm along the X, Y and Z axes, respectively. The interest of having this second stage enabling motion along X and Y (in addition to stage 9) is the possibility, offered by the piezoelectric technology, to generate vibration with small amplitude but high frequency (up to about 150, 150 and 8 Hz along X, Y and Z, respectively, accounting for the additional weight of about 6 kg placed on it. Between this piezoelectric table (8) and the lower sample holder (6) is placed a couple of stepper-motorized goniometers (7 ; OWIS, TPM 150-20-20-243) sharing the same center of rotation and enabling rotations of the sample around the axes X and Y in the range ±10°, with a repetability better than 0.01° per axis. These two rotations are in particular useful for alignment of the two samples, as seen in section III B.

The upper sample holder (5) is fixed on the lower end of a home-made 6-axis force/torque sensor (4) fully described in[34]. It enables measurement of the three forces along and of the three torques around the axes X, Y and Z, with resolutions 0.3, 0.4 and 0.1 mN for the respective forces and 1.0, 1.2 and 1.1µNm for the respective torques. The upper end of the force/torque sensor is fixed on a top plate (3) connected to the base plate (1) through precision guiding rods and bushings (2 ; Fibro GmbH). The top plate can be vertically moved to adjust the coarse position between samples using a precision drive (kollmorgen AKM31, not represented in Fig. 1). One distinctive feature of our force/torque sensor is that it is hollow so that, combined with a hollow upper sample holder (5), the contact interface can be observed from the top. The top plate (3) is thus equipped with a high resolution camera (12 ; Teledyne DALSA Genie Nano-GigE) and its objective (Qioptics optem fusion, with motorized zoom).

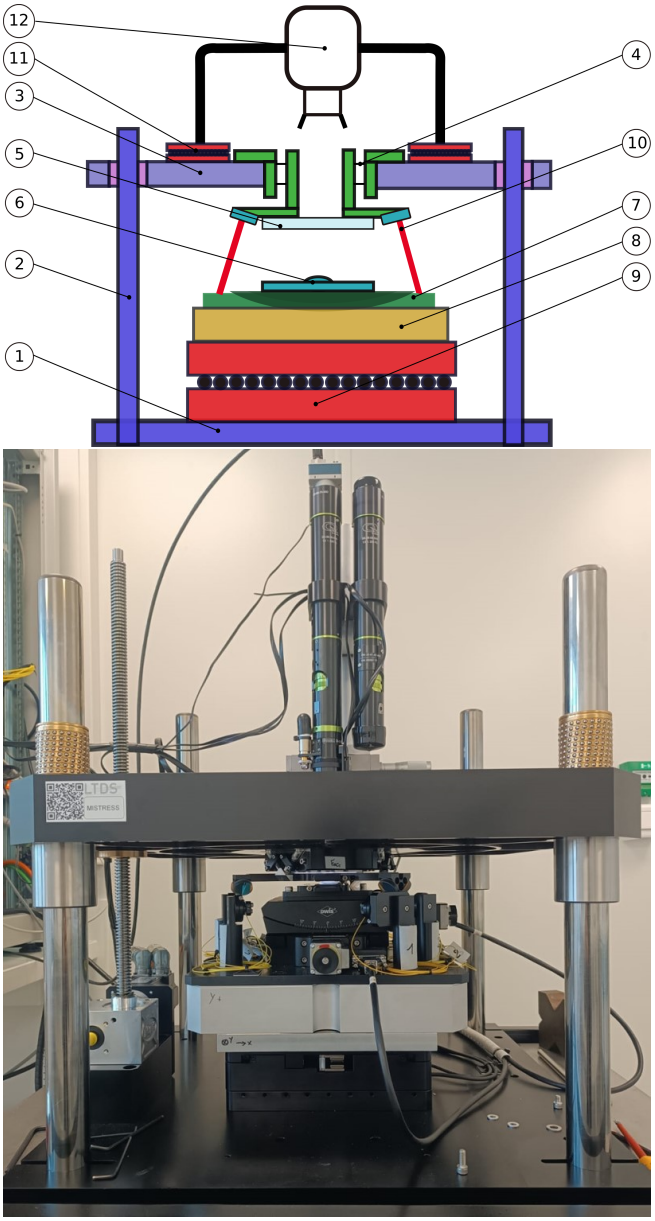

FIG. 1. Top (bottom): Sketch (photograph) of the instrument. (1) supporting table, (2) guiding rods, (3) top plate, (4) 6-axis force/torque sensor, (5) upper sample holder, (6) lower sample holder, (7)$\theta_X\theta_Y$ goniometers, (8) XYZ piezoelectric translation stage, (9) XY linear brushless servomotor translation stage, (10) 6-axis interferometer-based position sensor and (11) XY DC servomotor translation stage for the camera (12).

This large working distance optical system is placed on a XY motorized table (11 ; Newport) to center the image on the region of interest. The optical set up offers 4112×3008 pixels images of the contact interface with a pixel size down to 1 µm/pixel, and a field of view ranging from 3×4 to 9×12 mm^2.

The six-axes relative motion between the upper sample holder and the top plane of the piezoelectric table (three

translations along and three rotations around the X, Y and Z axes) is measured using six interferometers (10 ; Attocube IDS-3010) disposed in a stewart-platform-like fashion. The six interferometers are fixed on the plane connecting the piezoelectric stage (8) and the goniometers (7). The beam of each interferometer points on a precision flat mirror with planeity better than $\lambda/20$, fixed on the upper sample holder (5). This sensor enables measurements of translation amplitudes in the range ± 10 mm with a resolution better than 1 nm. Note that the measured motion does not include the rotations imposed by the goniometers, a choice related to the fact that, once the samples are aligned, these rotations are meant to remain constant during the subsequent contact mechanics experiments.

B. Real time control design and measurements

All measurements and control are performed through a control PC connected to a real time controller and a FPGA target (Field Programable Gate Array, NI-CRIO 9037 FPGA). This architecture allows us to have real time behavior for closed loop control, low pass filtering and lock-in functionality at a reasonable cost and with real time behavior. It also allows easily different control mode with no hardware change. This architecture is described in the fig 2.

The position information from the force sensor (Capacitive displacement sensor MCC10 and conditionning with Fogale MC900) is acquired through six 24-bits delta sigma analog to digital converters (NI 9239). The 1 x 6 vector signal is then multiplied by the 6 x 6 force matrix Kf obtained during force calibration to give the 1 x 6 Force vector (3 forces and 3 moments). The 6 signal received from the interferometers measurements are in the Aquad B form and are acquired through two NI9401 acquisition counters. This 1 x 6 vector is multiplied by the 6 x 6 displacement matrix Kd directly obtained with an inverse kinematic transformation from the known position of the interferometers. These calibrations matrix are given to the FPGA board after their rotations corrections when the program launch.

These signals are then low pass filtered at a frequency of $80Hz$ before being transmitted to the closed loop function. This function outputs the signal that drives the piezo vertical position, using a NI-9260 digital to analog converter. This function can act in 3 different manners : as an open loop, the output signal being received by the RT controler, as a Force closed loop (the output aiming to control the actual normal load to a setpoint received from the RT target), or as a displacement closed loop control (the output aiming to set the vertical displacement to a set point received from the RT controller). Each mode uses a defined set of parameters for the PID loop. This working mode of the PID loop, as the parameters driving the behavior of the loop can be changed in live during tests.

Before reaching the digital to analog converter that feed the input of the piezo amplifier, a sinusoidal numerical signal can be added to the output of the PID loop. This function is both controlled in frequency and amplitude, and allows the contact interface to receive a known dynamic excitation. The measured force and displacement raw signals, as the numerical sinusoidal function are fed into a multi channel Lock-in function. This function outputs the amplitude and phase of the force and displacement signals in relation with the input sinusoidal function. It is therefore possible to calculate the ratio between force and displacement, both in gain and phase at a controlled frequency, allowing the user to have a dynamic characterisation of the interface, in relation with the stiffness and viscosity of the interface.

All constant parameters are stored in a file and transmitted to the FPGA program at it starts. These include the values of the different frequencies used by the low pass filters, the values of the different PID parameters used during the different modes of the closed loop control, etc... During a tests, values are transferred from the FPGA to PC (the RT controller managing the formating of these values). These values include : raw signal from force and displacement sensor, filtered signal from force and displacement sensors, gains and phases output from lock in functions, PID output values.

III. CALIBRATION AND ALIGNMENT

A. Calibration of the displacement and force sensors

The 6×6 matrix K_d, that converts the six outputs distances of the six interferometers into the three displacements and three rotation angles of the upper sample holder with respect to the piezoelectric table, is obtained from a geometric transformation based on the known positions and orientations of the interferometers. No change of units is involved because the interferometers outputs are absolute distances to their mirrors. The displacements and angles are expressed in an arbitrary orthonormal frame, $(\mathbf{x}_d, \mathbf{y}_d, \mathbf{z}_d)$.

The 6×6 matrix K_f, that converts the six output voltages of the six capacitive sensors into the three forces and three torques applied to the upper sample holder, is obtained through a calibration procedure described in[34] (K_f of the present sensor is provided in appendix therein). The calibration involves application of known forces (using dead weights and pulleys when necessary) in many different directions. The matrix K_f is the matrix that best captures, in the least square sense, the observed relationship between all couples of input and output vectors. It is expressed in an arbitrary orthonormal frame, $(\mathbf{x}_f, \mathbf{y}_f, \mathbf{z}_f)$.

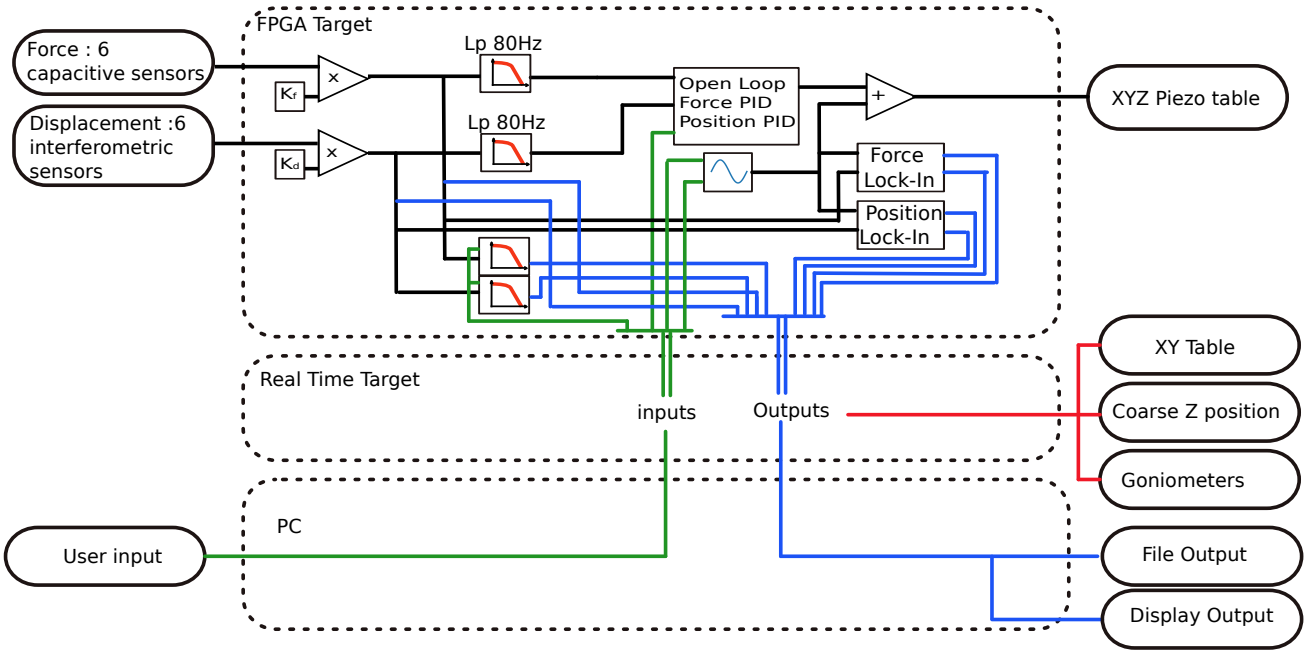

FIG. 2. Schematic view of the FPGA, real time and PC loops of the control of the bench. All acquired signals , as images acquired through the camera are displayed on screen during the test and can be recorded on a file for post processing. The user can choose to apply parameters to the experiment in "live mode", or use a sequence player to allow automated tests.

B. Alignment between sensors and actuators

To facilitate the interpretation of contact mechanics experiments, it is desirable to express the force and displacement measurements within the same frame as the actuation. To do this, we first define a reference frame, $(\mathbf{x}, \mathbf{y}, \mathbf{z})$ as follows. $\mathbf{x}$ and $\mathbf{y}$ correspond to the two axes of the motorized XY translation stage (label 9 in Fig. 1), while $\mathbf{z}$ is the axis that makes $(\mathbf{x}, \mathbf{y}, \mathbf{z})$ orthonormal. By construction of the instrument, the three axes of the XYZ piezoelectric stage (label 8), as well as the two rotation axes X and Y of the goniometers, are aligned with the axes of the frame $(\mathbf{x}, \mathbf{y}, \mathbf{z})$. Determination of the rotations that exist between $(\mathbf{x}_d, \mathbf{y}_d, \mathbf{z}_d)$, $(\mathbf{x}_f, \mathbf{y}_f, \mathbf{z}_f)$ and $(\mathbf{x}, \mathbf{y}, \mathbf{z})$ is made through the following three steps.

The first step is to determine the rotation angles between the actuation frame $(\mathbf{x}, \mathbf{y}, \mathbf{z})$ and the displacement sensor's frame $(\mathbf{x}_d, \mathbf{y}_d, \mathbf{z}_d)$. To do so, we first perform four linear motions of amplitude 1 mm with the motorised XY table, along the four directions $\mathbf{x}$, $-\mathbf{x}$, $\mathbf{y}$ and $-\mathbf{y}$, in the absence of any contact between the two sample holders. If the actuation and displacement frames were perfectly aligned, the measured displacements would have vanishing components along $\mathbf{y}_d$ and $\mathbf{z}_d$ (resp. $\mathbf{x}_d$ and $\mathbf{z}_d$) when moving along $\mathbf{x}$ or $-\mathbf{x}$ (resp. $\mathbf{y}$ or $-\mathbf{y}$). Instead, all these components (x_d, y_d and z_d) are found to vary linearly with, e.g., typical amplitudes 3 µm for z_d over 1 mm motion along $\mathbf{x}$. To eliminate such variations, we successively multiply the conversion matrix, K_d, by three rotation matrices: one with axis $\mathbf{z}_d$ and angle ψ_d calculated from the slope $\frac{\partial x_d}{\partial y_d}$; one with axis $\mathbf{x}_d$ and angle θ_d calculated from the slope $\frac{\partial z_d}{\partial y_d}$; one with axis $\mathbf{y}_d$ and angle ϕ_d calculated from the slope $\frac{\partial z_d}{\partial x_d}$. After those multiplications, the displacement components vary by less than 0.05 µm over displacements of 1 mm, indicating that the actuation and displacement frames are now aligned to better than 0.003°.

The second step consists in aligning the lower sample holder in a plane parallel to the plane $(\mathbf{x}, \mathbf{y})$. A steel sphere is placed in the upper sample holder, while a glass plate is place in the lower sample holder. A contact is then formed between the sphere and the plate, under a constant force along the axis $\mathbf{z}_f$, F_{z_f}=0.1 N, enforced through a feedback loop. Then, four linear motions of amplitude 1 mm are imposed to the lower sample holder with the motorised XY table, along the four directions $\mathbf{x}$, $-\mathbf{x}$, $\mathbf{y}$ and $-\mathbf{y}$. Because the lower sample holder is not parallel to $(\mathbf{x}, \mathbf{y})$, the vertical motion (along $\mathbf{z}$) is not constant, but varies linearly during the motions to keep F_{z_f} constant. To eliminate such an unwanted motion, we rotate both goniometers by angles calculated from $\frac{\partial z}{\partial y}$ around $\mathbf{x}$ and from $\frac{\partial z}{\partial x}$ around $\mathbf{y}$. Repeating the four motions in this rotated configuration yielded displacements along $\mathbf{z}$ smaller than 0.1 µm over horizontal displacements of 1 mm, showing that the lower sample holder is aligned with the displacement frame to better than 0.006°.

The third step is to determine the rotation angles between the actuation frame, $(\mathbf{x}, \mathbf{y}, \mathbf{z})$, and the frame of the force sensor, $(\mathbf{x}_f, \mathbf{y}_f, \mathbf{z}_f)$. To do so, we first insert a reference single-axis force sensor between the upper plane of the goniometers (label 7 in Fig.1) and the

lower sample holder (6). The sensor is attached on both ends using dedicated supports ensuring orthogonality of its measurement axis with the actuation plane $(\mathbf{x}, \mathbf{y})$. We then place an elastomer sphere (radius of curvature 9.42 mm, polydimethylsiloxane Sylgard 184, prepared as prescribed in[35]) in the upper sample holder and a glass plate in the lower sample holder.

The contact is generated at constant deformation by fixing the z position of the piezoelectric table resulting in a normal force of the order of 0.5 N. The sample is sheared along $\mathbf{x}$, $-\mathbf{x}$, $\mathbf{y}$ and $-\mathbf{y}$ directions a distance of 1 mm at 0.1 mm/s keeping z constant. We defined the adimensional parameter δ as the difference between the force measured by each sensor normalized by the force measured by the calibration sensor. This is

$$\delta = \frac{F_c - F_z}{F_c} \tag{1}$$

where F_c and F_z are the forces measured by the calibration sensor and the 6-axis force sensor respectively. Figure 3(a) and (b) shows the difference in the measure between both sensors as a function of the tangential force along X and Y respectively. In both cases the black curve shows the results of the experiments before the alignment, exhibiting a linear dependence with the tangential force in the respective shear direction. The correction is performed by rotating the transformation matrix of the 6-axis force sensor. The rotation angles are calculated so as to minimize δ. At the end of this procedure the calibration force sensor and the support are removed from the setup.

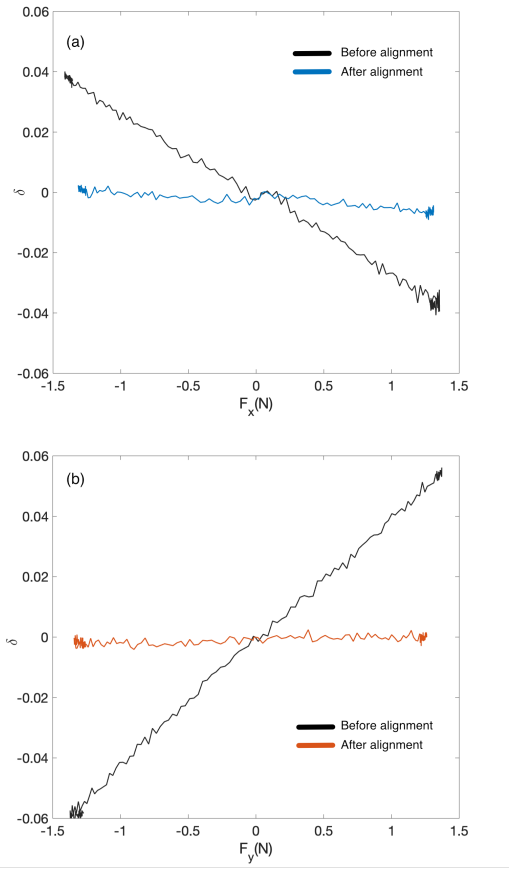

FIG. 3. Force sensor alignment. Evolution of δ as a function of the tangential forces, F_x (panel a) and F_y (panel b). Black lines are before step three of the alignment procedure, while colored curves are after alignment, where δ is as small as 0.5%.

IV. ILLUSTRATION EXPERIMENTS

A. Vibration-based detection of first contact

Detecting the very first contact between two approaching surfaces is a technological challenge, both for natural contacts and mechanical testing like nano-indentation or atomic force microscopy. Except for specifically-prepared ideally sharp indentors (eg Vickers), first contact can be modelled as the contact between a sphere and a plane. In such a case, the contact stiffness vanishes at small indentations, so that the normal force increases sub-linearly with indentation. First contact can be detected only when the normal force is larger than the noise of the force measurement, causing a significant uncertainty on first contact detection. To circumvent this difficulty, vibrating the contact during indentation is sometimes used to enhance first contact detection.

Our instrument is particularly suitable to implement such vibration-aided first contact detection, because (i) the XYZ piezoelectric table enables application of vibrations up to several tens of Hz and (ii) the lockin function embedded into the FPGA enables detection of minute oscillations in the outputs of the force or displacement sensors in noisy environments. In this context, we performed two indentation experiments between a PDMS sphere of curvature radius 500 µm (similar to those used in[36]) and fixed in the lower sample holder, and a glass plate, fixed in the upper sample holder. The first indentation experiment was performed as in[37], through a step-like motion with an average velocity of 0.028 µm/s. At each indentation step, a picture of the interface is taken, from which the contact area can be measured, as in. The second indentation experiment is performed in the same way, but an additional vibration of frequency 10 Hz and amplitude 0.9 µm is applied along the normal of the contact.

The contact area extracted from the images serves as the objective quantity to decide whether a contact exists between the two surfaces. This area is plotted in black in Fig. 4 (for both experiments), as a function of the imposed vertical displacement of the sphere, z. The almost perfect overlapping of the contact area evolution in both experiments demonstrates that vibration does not induce any noticeable modification of the mechanics of the contact. Note that the point where the contact area

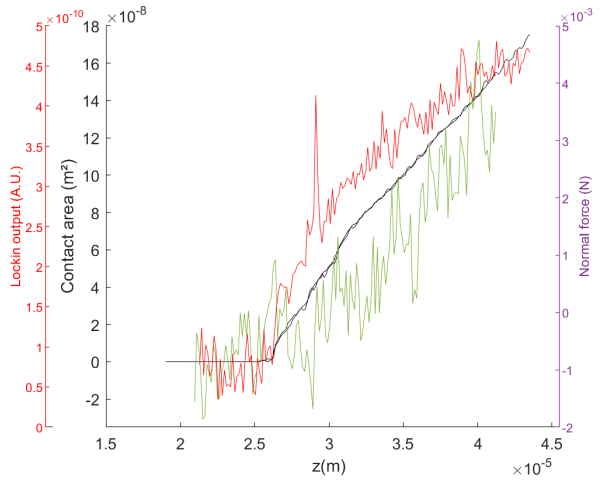

FIG. 4. Evolutions of the normal force (green curve, purple axis), contact area (black) and output of the lockin (red) as a function of the normal displacement, during progressive indentation of a PDMS sphere of radius 500 µmµm against a glass plate. Two experiments were performed, with or without an additional vibration (10 Hz, 0.9 µm) along the vertical axis. Normal force: without vibration. Lockin output: with vibration. Contact area: the two almost identical lines are with and without vibration.

becomes finite (the first contact that is looked for) has been used to define the origin of the horizontal axis.

The green curve in Fig. 4 shows the evolution of the normal force as z increases, in the un-vibrated indentation experiment. When the contact is not formed yet (z <0), the normal force is constant around 0, decorated by a measurement noise of typical amplitude ±1 mN. Thus, any true contact force smaller than about 1 mN cannot be distinguished from the noise, so that first contact cannot be detected. Such detection becomes possible only when the curves emerges from the noise, i.e., for $z \gtrsim$10 µm. As can be seen from Fig. 4, such detection occurs only when the contact area is already about 0.05 mm^2.

Let us now consider, as the red curve in Fig. 4, the output of the lockin modulus for the vibrated indentation. Note that the output is given in arbitrary units, because it depends on the unit of the sine signal used in the lockin multiplication step. The lockin output has a similar behaviour as the normal force. It is a noisy constant about $0\pm0.5\times10^{-10}$ in the absence of contact, and then an increasing function of z when the contact grows. Figure 4 shows that the lockin output emerges from the noise for $z \gtrsim$0.5 µm, i.e. only one step after contact detection from the images, and in any case much earlier than based on the normal force.

These results demonstrate that minute vibration of the contact, coupled with a lockin-based monitoring of the force component at the vibration frequency, is an efficient way of detecting the slightest contact between two solids. The sensitivity of such detection is comparable to that of contact imaging, but can potentially be accessed at a much faster rate than that of image analysis-based contact identification.

B. Alignment and imaging of contact between nominally flat surfaces

For sphere-plane contacts, the alignment procedure described in section III B is fully sufficient. In contrast, additional steps are required when dealing with two nominally flat surfaces, in order to create spatially homogeneous contacts. Indeed, (i) the upper sample holder is not perfectly parallel to the lower sample holder, and (ii) the flat sample may not have a perfectly constant thickness. To create homogeneous contacts, one needs to adjust, for each sample, the angles of the goniometers.

Figure 5 illustrates the impact of such an alignment on the example of a glass plate in the upper sample holder and a flat but rough PDMS block in the lower sample holder. The roughness takes the form of an array of spherical caps with all the same radius of curvature (500 µm), but with different height distributions (Dirac or exponential distributions in Figure 5). These surfaces are able to form, once in contact with a glass plate, so-called metainterfaces, the tribological behaviour of which can be finely tuned (see ref[36]).

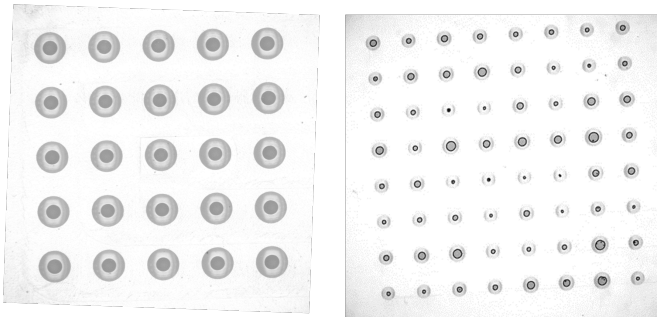

FIG. 5. Two typical examples of metainterfaces, based on model rough PDMS surfaces, after suitable alignment with a glass plate. Left: array of spherical caps with all the same height (Dirac distribution of heighs). Right: similar array but with exponential distribution of heights. In both panels, the dark regions are where intimate contact occurs between the PDMS and glass, and the interdistance between microcontacts is 1.5 mm.

Other examples of contact images obtained using the present instrument can be found in Refs[34,36,37].

V. CONCLUSIONS

We developed a new tribometer specially build for the study of soft contacts. This instrument enables complex kinematics, involving displacement along 5 axis (3 translation and 2 rotations), with controlled velocities and accelerations. The mechanical response of the interface

can be monitored with a fine resolution, using a 6-axes force/torque sensor and a 6-axes displacement/rotation sensor. On top of that, a real time *in-situ* observation of the interface is possible through the use of a dedicated camera.

By combining such a complex kinematic and the wide range of accessible measurements, the developed tribometer enables after calibration and alignment of the force and displacement sensors to investigate a large panel of soft contact submitted to very diverse mechanical solicitations.

In particular, this device could be used for:

- detect very finely the apparition of contact between two solid, by taking advantage of the real time actuation/monitoring of the forces (see section IV A).
- studying the mechanical behaviour of plane on plane rough contacts by combining the 6-axes force/torque measurements and the rotation of one of the surface (see section IV B and Ref[36])
- observing the interplay between adhesion and friction on the tribological response of a soft interface submitted to a complex kinematic, by combining the 3 translation actuators and the 6-axes force/torque measurements.
- exploring the adhesion instabilities of a sphere-plane contact, using the various feedback-loop dynamic controls over the actuators

These are only a few examples of what could be explored using this very versatile instrument.

ACKNOWLEDGMENTS

This work was supported by the LABEX iMUST (ANR-10-LABX-0064) of Université de Lyon, within the program "Investissements d'Avenir" (ANR-11-IDEX-0007) operated by the French National Research Agency (ANR). It was also supported by ANR through grant ANR-18-CE08-0011 (project PROMETAF).

[1] Jay Worobets and John William Wannop. Influence of basketball shoe mass, outsole traction, and forefoot bending stiffness on three athletic movements. *Sports Biomechanics*, 14(3):351–360, 2015.

[2] Ari J. Tuononen. Digital Image Correlation to analyse stick–slip behaviour of tyre tread block. *Tribology International*, 69:70–76, January 2014.

[3] J. Scheibert, S. Leurent, A. Prevost, and G. Debrégeas. The Role of Fingerprints in the Coding of Tactile Information Probed with a Biomimetic Sensor. *Science*, 323(5920):1503–1506, March 2009.

[4] A. J. Spiers, B. Calli, and A. M. Dollar. Variable-Friction Finger Surfaces to Enable Within-Hand Manipulation via Gripping and Sliding. *IEEE Robotics and Automation Letters*, 3(4):4116–4123, 2018.

[5] René A de Wijk, Lina Engelen, and Jon F Prinz. The role of intra-oral manipulation in the perception of sensory attributes. *Appetite*, 40(1):1–7, February 2003.

[6] Riad Sahli, Aubin Prot, Anle Wang, Martin H. Müser, Michal Piovarči, Piotr Didyk, and Roland Bennewitz. Tactile perception of randomly rough surfaces. *Scientific Reports*, 10(1):15800, September 2020.

[7] A. I. Vakis, V. A. Yastrebov, J. Scheibert, L. Nicola, D. Dini, C. Minfray, A. Almqvist, M. Paggi, S. Lee, G. Limbert, J. F. Molinari, G. Anciaux, R. Aghababaei, S. Echeverri Restrepo, A. Papangelo, A. Cammarata, P. Nicolini, C. Putignano, G. Carbone, S. Stupkiewicz, J. Lengiewicz, G. Costagliola, F. Bosia, R. Guarino, N. M. Pugno, M. H. Müser, and M. Ciavarella. Modeling and simulation in tribology across scales: An overview. *Tribology International*, 125:169 – 199, 2018.

[8] Bart Weber, Julien Scheibert, Maarten P. de Boer, and Ali Dhinojwala. Experimental insights into adhesion and friction between nominally dry rough surfaces. *MRS Bulletin*, 47(12):1237–1246, December 2022.

[9] Martin H. Müser, Wolf B. Dapp, Romain Bugnicourt, Philippe Sainsot, Nicolas Lesaffre, Ton A. Lubrecht, Bo N. J. Persson, Kathryn Harris, Alexander Bennett, Kyle Schulze, Sean Rohde, Peter Ifju, W. Gregory Sawyer, Thomas Angelini, Hossein Ashtari Esfahani, Mahmoud Kadkhodaei, Saleh Akbarzadeh, Jiunn-Jong Wu, Georg Vorlaufer, András Vernes, Soheil Solhjoo, Antonis I. Vakis, Robert L. Jackson, Yang Xu, Jeffrey Streator, Amir Rostami, Daniele Dini, Simon Medina, Giuseppe Carbone, Francesco Bottiglione, Luciano Afferrante, Joseph Monti, Lars Pastewka, Mark O. Robbins, and James A. Greenwood. Meeting the Contact-Mechanics Challenge. *Tribology Letters*, 65:118, December 2017.

[10] Riad Sahli, Gaël Pallares, Christophe Ducottet, Imed Eddine Ben Ali, Samer Al Akhrass, Matthieu Guibert, and Julien Scheibert. Evolution of real contact area under shear and the value of static friction of soft materials. *Proceedings of the National Academy of Sciences of the USA*, 115:471–176, 2018.

[11] T. Baumberger, C. Caroli, and O. Ronsin. Self-healing slip pulses and the friction of gelatin gels. *The European Physical Journal E - Soft Matter*, 11(1):85–93, May 2003.

[12] Julia Nase, Anke Lindner, and Costantino Creton. Pattern Formation during Deformation of a Confined Viscoelastic Layer: From a Viscous Liquid to a Soft Elastic Solid. *Physical Review Letters*, 101(7):074503, August 2008.

[13] J. F. Waters and P. R. Guduru. Mode-mixity-dependent adhesive contact of a sphere on a plane surface. *Proceedings of the Royal Society A: Mathematical, Physical and Engineering Sciences*, 466(2117):1303–1325, May 2010.

[14] A. Prevost, J. Scheibert, and G. Debrégeas. Probing the micromechanics of a multi-contact interface at the onset of frictional sliding. *The European Physical Journal E*, 36(2), February 2013.

[15] Benoit Delhaye, Philippe Lefevre, and Jean-Louis Thonnard. Dynamics of fingertip contact during the onset of tangential slip. *Journal of the Royal Society Interface*, 11(100):20140698, November 2014. WOS:000344533800004.

[16] Marie-Julie Dalbe, Pierre-Philippe Cortet, Matteo Ciccotti, Loïc Vanel, and Stéphane Santucci. Multiscale Stick-Slip Dynamics of Adhesive Tape Peeling. *Physical Review Letters*, 115(12), September 2015.

[17] Alexander J. McGhee, Angela A. Pitenis, Alexander I. Bennett, Kathryn L. Harris, Kyle D. Schulze, Juan Manuel Urueña, Peter G. Ifju, Thomas E. Angelini, Martin H. Müser, and W. Gregory Sawyer. Contact and Deformation of Randomly Rough Surfaces with Varying Root-Mean-Square Gradient. *Tribology Letters*, 65(4):157, November 2017.

[18] R. Sahli, G. Pallares, A. Papangelo, M. Ciavarella, C. Ducottet, N. Ponthus, and J. Scheibert. Shear-Induced Anisotropy in Rough Elastomer Contact. *Physical Review Letters*, 122:214301, May 2019.

[19] Carmine Putignano, Thomas Reddyhoff, Giuseppe Carbone, and Daniele Dini. Experimental Investigation of Viscoelastic Rolling Contacts: A Comparison with Theory. *Tribology Letters*, 51(1):105–113, July 2013.

[20] M Scaraggi and B N J Persson. Friction and universal contact

area law for randomly rough viscoelastic contacts. *Journal of Physics: Condensed Matter*, 27(10):105102, March 2015.

[21]Tooba Shoaib and Rosa M. Espinosa-Marzal. Influence of Loading Conditions and Temperature on Static Friction and Contact Aging of Hydrogels with Modulated Microstructures. *ACS Applied Materials & Interfaces*, 11(45):42722–42733, November 2019. Publisher: American Chemical Society.

[22]Yanling Yin, Shih-Fu Ling, and Yong Liu. A dynamic indentation method for characterizing soft incompressible viscoelastic materials. *Materials Science and Engineering: A*, 379(1):334–340, August 2004.

[23]G. Boyer, L. Laquièze, A. Le Bot, S. Laquièze, and H. Zahouani. Dynamic indentation on human skin in vivo: ageing effects. *Skin Research and Technology*, 15(1):55–67, February 2009. Publisher: John Wiley & Sons, Ltd.

[24]Aref Samadi-Dooki, George Z. Voyiadjis, and Rhett W. Stout. An Indirect Indentation Method for Evaluating the Linear Viscoelastic Properties of the Brain Tissue. *Journal of Biomechanical Engineering*, 139(061007), April 2017.

[25]K.J. Wahl, S.A.S. Asif, J.A. Greenwood, and K.L. Johnson. Oscillating adhesive contacts between micron-scale tips and compliant polymers. *Journal of Colloid and Interface Science*, 296(1):178–188, April 2006.

[26]E. Charrault, C. Gauthier, P. Marie, and R. Schirrer. Experimental and Theoretical Analysis of a Dynamic JKR Contact. *Langmuir*, 25(10):5847–5854, May 2009. Publisher: American Chemical Society.

[27]J. Benad, K. Nakano, V. L. Popov, and M. Popov. Active control of friction by transverse oscillations. *Friction*, 7(1):74–85, February 2019.

[28]L. Dorogin, A. Tiwari, C. Rotella, P. Mangiagalli, and B. N. J. Persson. Role of Preload in Adhesion of Rough Surfaces. *Physical Review Letters*, 118(23):238001, June 2017.

[29]V. V. Aleshin and O. Bou Matar. Solution to the frictional contact problem via the method of memory diagrams for general 3D loading histories. *Physical Mesomechanics*, 19(2):130–135, April 2016.

[30]M. Popov, V.L. Popov, and R. Pohrt. Relaxation damping in oscillating contacts. *Scientific Reports*, 5(1), December 2015.

[31]Z. Mané, J.-L. Loubet, C. Guerret, L. Guy, O. Sanseau, L. Odoni, L. Vanel, D.R. Long, and P. Sotta. A new rotary tribometer to study the wear of reinforced rubber materials. *4th UK-China Tribology*, 306(1):149–160, August 2013.

[32]Nick Gravish, Matt Wilkinson, and Kellar Autumn. Frictional and elastic energy in gecko adhesive detachment. *Journal of The Royal Society Interface*, 5(20):339–348, March 2008. Publisher: Royal Society.

[33]Janine C. Mergel, Riad Sahli, Julien Scheibert, and Roger A. Sauer. Continuum contact models for coupled adhesion and friction. *The Journal of Adhesion*, 95(12):1101–1133, 2019.

[34]M. Guibert, C. Oliver, T. Durand, T. Le Mogne, A. Le Bot, D. Dalmas, J. Scheibert, and J. Fontaine. A versatile flexure-based six-axis force/torque sensor and its application to tribology. *Review of Scientific Instruments*, 92(8):085002, 2021.

[35]Emilie Delplanque, Antoine Aymard, Davy Dalmas, and Julien Scheibert. Solving curing-protocol-dependent shape errors in PDMS replication. *Journal of Micromechanics and Microengineering*, 32(4):045006, March 2022.

[36]Antoine Aymard, Emilie Delplanque, Davy Dalmas, and Julien Scheibert. Designing metainterfaces with specified friction laws. *Science*, 383(6679):200–204, 2024. _eprint: https://www.science.org/doi/pdf/10.1126/science.adk4234.

[37]C. Oliver, D. Dalmas, and J. Scheibert. Adhesion in soft contacts is minimum beyond a critical shear displacement. *Journal of the Mechanics and Physics of Solids*, 181:105445, 2023.